2025 IEEE/SICE International Symposium on System Integration (SII)
January 21-24, 2025, Munich, Germany

Theoretical Research of Tactile Shape Sensor for Complex Surfaces Based on Fiber-Optic Distributed Sensors

Zeyu Long, Hidefumi Wakamatsu, Yoshiharu Iwata

Abstract— **Tactile shape sensor is a crucial research focus in the field of soft robotics, and many researchers have developed intelligent tactile shape sensors. However, current research on tactile shape sensors predominantly focuses on simple shapes such as bending and twisting, neglecting a common but significant shapes – concave-convex shapes. This study introduces a tactile shape sensor based on Fiber-Optic distributed sensors, and it utilizes traditional optimization algorithms, avoiding the influence of training data associated with machine learning. In this research, we propose a method to predict shapes using strain data from fibers. The validation of this prediction method is primarily theoretical, conducted through simulations. This research conducts beyond validating basic shapes like bending, twisting, and stretching, and also includes various complex concave-convex shapes, single-point pressing, multi-point pressing (3 points), and reverse pressing (2 points) in case studies. In ideal conditions, the predicted shapes match the set sample shapes perfectly.**

I. INTRODUCTION

Within the realm of soft robotics, tactile sensors have become a highly prominent research focus. Tactile sensors are devices designed to detect and measure physical contact or touch. These sensors are sensitive to forces, pressure, vibrations, or any other mechanical stimuli[1]. Tactile sensors possess advantages such as flexibility and wearability, making them particularly well-suited for applications in health monitoring and the monitoring of deformable soft robots[2]. Many researchers have designed tactile sensors for monitoring parameters such as heart rate and temperature. Similarly, many researchers also have developed tactile sensors for shape detection[3].

Tactile shape sensors are a type of tactile sensors capable of detecting shapes. The challenge in research lies in the design of the structure and shape reconstruction. Shah et al. developed a tactile shape sensor based on a biphasic gallium indium alloy (bGaIn) and successfully predicted common bending shapes[4]. However, the fabrication of this method is intricate, and the outcomes indicate its capability to predict only some simple bending shapes. Costi et al. proposed a barometric tactile sensor[5]. The fabrication of this tactile sensor is also challenging, and the high air-tight chambers are susceptible to environmental influences. Importantly, it cannot fully predict the shape of contact but the position of contact points. Addressing the fabrication challenges of tactile sensors may be achieved by using already commercialized technologies. These mature technologies are more cost-effective. Utilizing them directly in designing tactile sensors could streamline fabrication processes, facilitating future mass production.

Z. Long, H. Wakamatsu, and Y. Iwata are with the Dept. of Materials & Manufacturing Science, Osaka University, 2-1 Yamadaoka, Suita, Osaka 565-0871, Japan {zeyu.long, wakamatu, iwata}@mapse.eng.osaka-u.ac.jp

Fiber-Optic distributed sensors, as a mature sensing technique, utilizes optical fibers as a foundation to detect parameters such as temperature, strain, and vibrations. It has found widespread applications in fields like construction engineering and agriculture[6]. As a sensor, Fiber-Optic distributed sensors offer advantages such as small size and high sensitivity.

In this study, a tactile shape sensor based on Fiber-Optic distributed sensors is proposed. The Fiber-Optic distributed sensors used in this research is capable of detecting strain. For ease of expression, this sensor is abbreviated as FBSS (Fiber-Based Shape Sensor). In FBSS, fibers are arranged in a grid pattern on both sides of a fabric, and the overall structure resembles sheets. When FBSS is in contact, it undergoes deformation, causing changes in the strain data of the embedded fibers. We reconstruct the shape of FBSS using the strain data to achieve shape detection. This study provides a theoretical foundation for this concept, exploring the possibility of shape reconstruction through the distribution of strain data. The algorithm employed in this theoretical approach does not use machine learning but relies on traditional optimization algorithms. We believe this approach is more reliable, as it maintains accuracy even with shape, which isn't included in training database.

The study is primarily divided into three phases: data preparation phase, shape prediction phase, and results presentation phase. In the data preparation phase, a discrete modeling method for FBSS is proposed. To deform it into a predefined sample shape, geometric constraints are applied. Subsequently, the total potential is minimized to compute the sample shape and derive the distribution of strain data. In the shape prediction phase, the modeling method is similar to the data preparation phase, but original constraints in data preparation phase are removed, and strain data from the data preparation phase are introduced as new constraints. The total potential is minimized again to compute and predict the shape. Finally, the predicted shape is compared with the sample shape to assess reliability. In the results presentation phase, various sample shapes, including basic bending, twisting, stretching, as well as more complex surface, are systematically presented and analyzed.

Compared to other research on tactile shape sensors, our research possesses the following advantages. Fiber-Optic distributed sensors as a mature and commercially available strain sensing technology, utilizing this as the foundation, the fabrication of FBSS is remarkably straightforward—simply arranging fibers on fabrics completes the production process.

Moreover, fibers are extremely thin, some even smaller than 1mm. Consequently, FBSS are thin and soft, exerting minimal impact on the motion of the object being detected. Additionally, while many tactile shape sensors predominantly accommodate simple shapes like bending, twisting, and stretching, they often fall short in addressing another common but complex shape—concave-convex shape. For surfaces, concave-convex shapes are prevalent, making it essential for tactile shape sensors. Taking the field of health monitoring, where tactile shape sensors are frequently applied, as an example, the shapes of muscles, protruding skeletal features, and facial characteristics are often concave-convex in nature. Thus, the ability to accurately predict concave-convex shapes becomes crucial. This study can address concave-convex shapes, which other research has not taken into consideration.

There are other studies that also use fibers as the basis for tactile shape sensors, such as the one proposed by Tian et al. [7]. However, this study only employed two circular fibers, limiting its ability to correspond to simple bending and twisting shapes, without accommodating concave-convex shapes. Moreover, this method utilizes a machine learning algorithm, which lacks a clear and explicit algorithm and may struggle with shapes that have not been trained. Zhang et al. also utilized fibers to design tactile shape sensors[8]. However they also can only correspond to simple bending shapes. In comparison with these fiber-based studies, the strengths of our research lie in having a clear and stable algorithm. Additionally, our study not only caters to simple shapes like bending but also addresses concave-convex shapes. This capability is crucial for tactile shape sensors.

Given these advantages, FBSS holds potential applications. Firstly, in the field of health monitoring, such as monitoring the shape of Buffalo Hump, which refers to the abnormal accumulation of soft tissue in the back caused by long-term steroid use, or monitoring the shape of the scapula. FBSS can effectively correspond to both of these typical convex shapes during the recovery process. On the other hands, FBSS is suitable for shape detection in deformable soft robots. Because FBSS overall structure is thin and soft, it does not significantly interfere with the inherent movement of the robot.

II. DATA PREPARATION PHASE

The surface shape should be predicted using the method proposed in this study from actual measurement data. However, actual measurement data generally includes various errors. If there is an error between the shape predicted by the proposed method and the actual shape, it is difficult to determine whether it is due to imperfections in the proposed method or errors in the measured data. Therefore, in this study, we first prepare ideal pseudo-measurement data that does not contain any errors and use it to verify the validity of the proposed method. The data preparation phase is set up for this purpose.

The main purpose of this phase is to prepare strain data for subsequent shape prediction phase. We first propose a discrete modeling method for FBSS. Subsequently, specific geometric constraints are applied to deform it into a sample shape. Finally, the total potential is calculated, minimized to derive the shape, and strain data for this shape are then extracted. The overall arrangement of the discrete model for FBSS is illustrated in Fig.1.

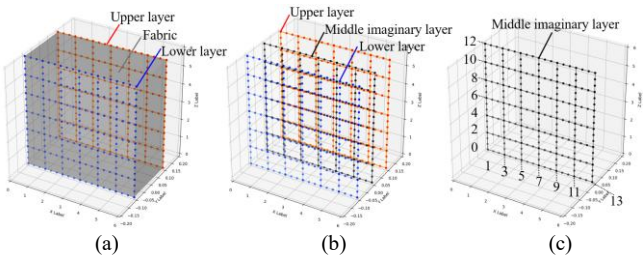

Figure 1. Diagram of FBSS

The FBSS discrete model consists of two layers of fiber nets, with each layer comprising 14 orthogonal fibers forming the net. Each fiber has 19 nodes, and the fibers, with a length of L, create a square of L x L. The gap between the two layers of fibers is $L/30$. In a physical prototype, these two layers of fibers would be adhered to opposite sides of a fabric as shown in Fig.1-(a), and the thickness of fabric is $L/30$, with the fabric omitted in the illustration. It is essential to note that, for better visualization, the proportion of the figure has been altered.

As this study aims to validate the reliability of the prediction method and provide a theoretical foundation for future practical experiments, the model has been idealized. Consequently, for this idealized model, the following preconditions have been established to facilitate more efficient modeling: Firstly, the intersections of the fiber net are connected without undergoing relative displacements. Secondly, there is no relative displacement between the fibers and the fabric. Thirdly, the thickness of the fabric remains constant.

In normal discrete model, discrete model nodes are independent. With the parameters set for the current FBSS, a total of 532 nodes would be required. However, building upon the aforementioned preconditions, we can devise a more intelligent model to reduce the number of nodes, significantly enhancing the computational speed of optimization calculations. Given that there is no relative displacement between the fibers and the fabric, and the thickness of the fabric remains constant, we only need to define a middle imaginary layer of the upper and lower layer, as depicted by the black section in the Fig.1-(b). This allows us to determine the coordinates of nodes on both sides. The increase in variables in optimization calculations often results in an exponential growth in computation time. Therefore, while modeling by defining the middle layer may sacrifice a small amount of precision, it leads to substantial time savings in optimization calculations. It is important to note that the middle layer is an imaginary layer and does not exist.

Therefore, the next step involves defining the coordinates of nodes on both sides by defining the middle layer. The fiber net consists of 14 fibers, and the definition for each fiber is independent. Each fiber has 19 nodes, which are defined by 19 local coordinate systems.

As shown in Fig.2, the definition of each fiber is comprised of local coordinate systems denoted as $M_{a,b}$-$\xi\eta\zeta$

where a means the number of a fiber and b means the number of a node of the fiber. Moreover, if a is an even number, the fiber is a vertical one, and if an odd number, a horizontal one, the numbering scheme for fibers is illustrated in Fig.1-(c). In these coordinate systems, the $\boldsymbol{\zeta}_{a,b}$-direction corresponds to the length direction. The node coordinates $\boldsymbol{m}_{0,i}$ of the point $M_{0,i}$ can be calculated sequentially, as shown in (1):

$$\boldsymbol{m}_{0,i} = \boldsymbol{m}_{0,0} + \sum_{j=1}^{i} \boldsymbol{\zeta}_{0,j} l(1+\varepsilon_{0,j}). \tag{1}$$

where l=L/18 represents the segment length between two nodes, and $\varepsilon_{0,j}$ represents the strain of a segment between points $M_{0,j\text{-}1}$ and $M_{0,j}$.

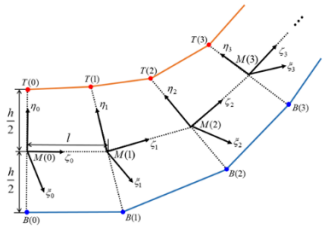

Figure 2. Discrete model based on local coordinate system

We use the origin as the starting point to define the initial vertical fiber 0 and horizontal fiber 1. However, in the subsequent definition of fiber coordinates, the initial coordinate vector $\boldsymbol{m}_{a,0}$ is no longer the origin (0,0,0) but the corresponding node coordinates on fibers 0 and 1. Taking fiber 2 as an example, the initial node coordinates of fiber 2 are located on node 3 of fiber 1. Therefore, $\boldsymbol{m}_{2,0}$=$\boldsymbol{m}_{1,3}$.

Next, the coordinates of the fiber nodes on both sides can be defined using the local coordinate system of the middle layer. Taking the η-direction as the defining direction for the fiber, and with a thickness of h, the calculation of the fiber node position vectors $\boldsymbol{t}_{0,i}$ and $\boldsymbol{b}_{0,i}$ for upper layer and lower layer points, $T_{0,i}$ and $B_{0,i}$,are given by (2). It is important to note that the thickness h remains constant.

$$\begin{cases} \boldsymbol{t}_{0,i} = \boldsymbol{m}_{0,i} + \dfrac{h}{2}\boldsymbol{\eta}_{0,i} \\ \boldsymbol{b}_{0,i} = \boldsymbol{m}_{0,i} - \dfrac{h}{2}\boldsymbol{\eta}_{0,i} \end{cases}. \tag{2}$$

Through (1), (2), similarly, we can define a total of 38 fibers across both layers. The coordinates of these fibers' nodes are defined based on local coordinate systems. As for the local coordinate systems, we define them using a concept similar to angular velocity.

As shown in Fig.3, we initially specify that the direction of the initial local coordinate system aligns with the global coordinate system, as shown in $M_{a,b}$-$\xi\eta\zeta$. Subsequently, for each $M_{a,b}$-$\xi\eta\zeta$ local coordinate system, we define a rotation vector $\boldsymbol{\omega}_{a,b}$. It is essential to note that $\boldsymbol{\omega}_{a,b}$ is not a unit vector. Following this, $M_{0,0}$-$\xi\eta\zeta$ rotates about the axis $\boldsymbol{\omega}_{0,0}$ by an angle equal to the magnitude of $\boldsymbol{\omega}_{0,0}$, resulting in $M_{0,1}$-$\xi\eta\zeta$. This process continues until $M_{0,i}$-$\xi\eta\zeta$. In this manner, by utilizing several rotation vectors $\boldsymbol{\omega}_{a,b}$, we can define the orientations of all local coordinate systems. The three coordinates of these rotation vectors $\boldsymbol{\omega}_{a,b}$ will be treated as variables and computed in the optimization calculations.

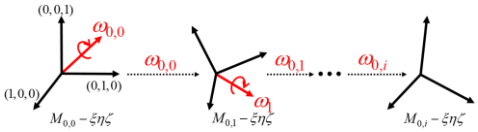

Figure 3. Rotation of local coordinate system

We defined local coordinates through several rotation vectors and subsequently used these local coordinate systems to define the node coordinates of the fibers in the upper and lower layers. Since each pair of fibers one from the upper layer and one from the lower layer, is independently defined, each fiber is essentially still entirely free; they are entirely independent and have not been woven into a net. To consolidate these fibers into a net, specific geometric constraints need to be applied. This geometric constraint stipulates that the coordinates of corresponding nodes on intersecting fibers must be identical. This essentially fixes the intersection points, preventing them from separating. Taking the intersection point of the fiber 2 and fiber 3 in the Fig.1 as an example, the geometric constraint is expressed as (3):

$$\begin{cases} \boldsymbol{\eta}_{2,3} = \boldsymbol{\eta}_{3,3} \\ \boldsymbol{m}_{2,3} = \boldsymbol{m}_{3,3} \end{cases}. \tag{3}$$

These two constraints ensure that the intersection points of the upper and lower layers are interconnected. After adding the aforementioned geometric constraints for each intersection point, the independent fibers are woven into a net, interconnecting with each other, preventing separation.

The aforementioned geometric constraints are invariant and shape-independent; they prevent the separation of intersection points regardless of the shape. However, to achieve the specified sample shape, additional specific geometric constraints need to be added. This study validated various sample shapes. In this section, bending shape is taken as an example. For the bending sample shape, the applied geometric constraints are outlined in (4), Its practical significance is to fix the two edges of FBSS and retract them by a distance of L/4, which will cause FBSS to bend in one direction.

$$\begin{cases} \boldsymbol{m}_{2i+1,0} = (0,\ 0,\ 3il) \\ \boldsymbol{m}_{2i+1,18} = (0.75L,\ 0,\ 3il) \end{cases} \quad (i = 0, \cdots, 6). \tag{4}$$

Finally, we need to formalize the total potential energy. The algorithm employed in this study is optimization calculation, and the objective function for optimization calculation is the total potential energy, as shown in (5):

$$U = U_{flex} + U_{tor} + U_{ext}. \tag{5}$$

U_{flex}, U_{tor} and U_{ext} respectively represent the flexural

potential energy, torsional potential energy and extensional potential energy. The specific calculation formulas for each potential are as (6), (7) and (8):

$$U_{flex} = \sum_{j=0}^{13}[\frac{R_f}{2}\cdot l\cdot\sum_{i=1}^{18}(\omega_{\xi,j,i}^2+\omega_{\eta,j,i}^2)], \tag{6}$$

$$U_{tor} = \sum_{j=0}^{13}[\frac{R_t}{2}\cdot l\cdot\sum_{i=1}^{18}\omega_{\zeta,j,i}^2], \tag{7}$$

$$U_{ext} = \sum_{j=0}^{13}[\frac{R_e}{2}\cdot l\cdot\sum_{i=1}^{18}\varepsilon_{j,i}^2]. \tag{8}$$

The essence of the computation method is, the calculation and summation of the potentials for each node on every fiber. The calculation of the extensional potential energy is relatively easy to understand. For the flexural potential energy and torsional potential energy, the ζ-axis was selected as the length direction during the modeling process. Therefore, the component along the ζ-axis of rotational vector $\boldsymbol{\omega}_{j,i}$, represented as $\boldsymbol{\omega}_{\zeta,j,i}$, only induces torsion. The components along the other two directions, $\boldsymbol{\xi}$ and $\boldsymbol{\eta}$, cause bending, leading to the derivations of (6) and (7). Where R_f, R_t, and R_e are the flexural rigidity, torsional rigidity, and extensional rigidity of the fiber, respectively.

The calculation of the total potential energy in this study is essentially the calculation of the total potential energy in the middle layer. The reason for not calculating the total potential of the upper and lower layers separately is for computational simplicity. The upper and lower layers are determined by the same local coordinate system, and the thickness remains constant. Since the thickness itself is relatively small compared to the length, the total potential energy of the middle layer is approximately the average of the potentials of the upper and lower layers. Therefore, choosing to calculate the total potential energy of the middle layer simplifies the steps with a minimal loss in computational accuracy.

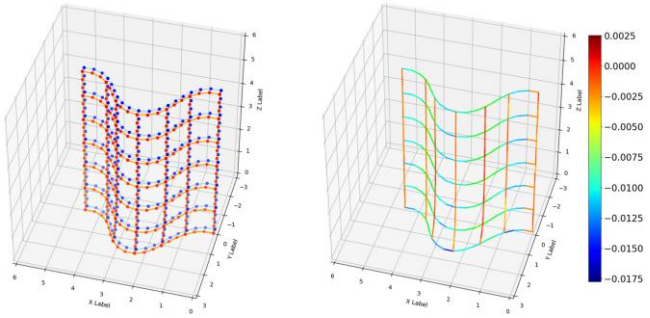

(a) Bending shape of FBSS (b) Strain distribution of bending shape

Figure 4. Computational result of bending shape

For the optimization calculation, we utilize the algorithm with the simplex method and the Lagrange multiplier method[9] as its core. We define (5) as the objective function and impose (3) and (4) as geometric constraints. With a total of 266 nodes, each node having three variables, there are a total of 798 variables. The final computation took approximately 5 hours on a CPU with a model number of Core i7-1260P. We made a C language program to perform this optimization computation. The resulting computation is shown on Fig.4.

Fig.4-(a) displays the shape of FBSS, showing the positions of the fiber net in both the upper and lower layers. Red represents the upper layer fibers, while blue represents the lower layer fibers. The shape difference between the upper and lower layers is minimal. As depicted in the figure, FBSS deforms into a bending shape, and intuitively, this deformation aligns with objective perception. By using the coordinates of points in the upper and lower layers, we can calculate the strain distribution as follows:

$$\begin{cases} \varepsilon_{i,j}^{t,0} = \dfrac{|\boldsymbol{t}_{i,j}-\boldsymbol{t}_{i,j-1}|}{l}-1 \\ \varepsilon_{i,j}^{b,0} = \dfrac{|\boldsymbol{b}_{i,j}-\boldsymbol{b}_{i,j-1}|}{l}-1 \end{cases}. \tag{9}$$

Fig.4-(b) illustrates the strain distribution of the upper layer, where the strain along the vertical fibers is close to 0, and the compression is maximal in the central part of the horizontal fibers. Since displaying the strain distribution of two layers simultaneously would make the figure too cluttered, and the strain distribution among the upper and lower layers is nearly identical, only one layer is shown. These strain data represent the results of the data preparation phase and will be imported into the prediction calculation in the next phase.

III. SHAPE PREDICTION PHASE

In this phase, the data prepared in the data preparation phase will be used for prediction calculations, aiming to reconstruct the shape of FBSS. Taking the bending shape from the data preparation phase as an example, the modeling method in the shape prediction phase, as well as the geometric constraints (3) for interweaving fibers and the method for calculating total potential energy, are identical. The difference lies in the removal of geometric constraints (4), which were originally the constraints causing FBSS to deform into a bending shape. After removing these constraints, FBSS transforms back into a fiber net that can deform freely.

For the currently freely deformable FBSS, we import the strain data of upper and lower layer, $\varepsilon_{j,i}^{t,0}$ and $\varepsilon_{j,i}^{b,0}$, during the bending shape as constraints. Both of upper and lower layer, the strain at each node must be equal to the strain at the corresponding node during the bending shape, namely,

$$\begin{cases} \sum_{j=0}^{13}\sum_{i=1}^{18}(\varepsilon_{j,i}^{t}-\varepsilon_{j,i}^{t,0})^2 = 0 \\ \sum_{j=0}^{13}\sum_{i=1}^{18}(\varepsilon_{j,i}^{b}-\varepsilon_{j,i}^{b,0})^2 = 0 \end{cases}. \tag{10}$$

To satisfy (10), FBSS must deform to meet the requirements, ultimately forming a shape that also satisfies the minimum potential energy state, referred to as the predicted shape. The work of this section is to evaluate whether the predicted shape

aligns with the sample shape from the data preparation phase.

The prediction computation took approximately 1.5 hours, and the results are shown in Fig.5.

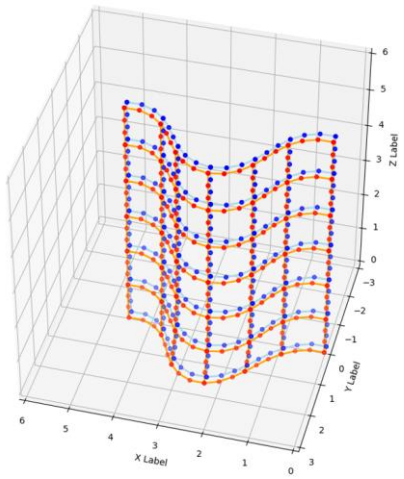

Figure 5. Prediction shape

From Fig.5, we can observe that the predicted shape is almost identical to the sample shape from the data preparation phase. We calculated the deviation distance *d* for each node. We define the error rate *Err=d/L*. Through calculations, the average and max error rate for this prediction is approximately 0.14% and 0.36%.

Based on the quantitative analysis of prediction errors and direct observation of the shape, we consider this prediction calculation successful, specifically for the bending shape. Despite the presence of a small amount of error, we attribute this to the precision settings of the optimization calculation. If the computational precision is increased, it will reduce this prediction error. The prediction method in this study can effectively constrain and reconstruct the shape of FBSS for bending shape. However, deformation of curved surfaces is complex, and additional case studies are required to ensure that this prediction method can accurately predict shapes for various curved surfaces.

IV. RESULTS PRESENTATION PHASE

Through the research in the previous two phase, we have established the basic feasibility of the current method for the arrangement of fibers and the prediction calculation method. It has proven successful in predicting bending shapes. In this section, we will conduct more case studies to validate the reliability of this method.

We defined six sample shapes, including basic bending, twisting, and stretching shapes, as well as more complex concave-convex shapes such as a single point press, multi-point press (3 points), and reverse press (2 points). Prediction calculations were performed for each of these six sample shapes, and the comparative results along with error rates are shown in Fig.6. As the shapes of the upper and lower layers are nearly identical, and presenting both makes observation challenging, only the shape and strain distribution of one layer are shown.

Through Fig. 6, we observe that overall, the predicted shapes closely match the sample shapes, with an average error rate of less than 1% and a maximum error rate of less than 3%. Among them, the prediction performance of bending shapes, twisting shapes, single point press, and reverse press shape is excellent, with almost no errors. However, the prediction results for stretching shapes and multi-point press shape, while maintaining a relatively low error rate, are still significantly higher than the other four shapes. We believe this is related to the precision of the optimization calculation settings.

The predictions for all six shapes are calculated with the same precision. However, stretching shapes and multi-point press shapes require higher precision. This is because both of these shapes include planar components, and the multi-point press shape, which is quasi-planar, lies within the small triangle formed by the three pressing points. Taking stretching shapes as an example, the overall flexural potential energy of the planar component is low, approaching a level close to 0. The minimal increase in flexural potential energy due to the slight bending of the stretched protruding part to the sides is extremely small. If the precision of the optimization calculation is not high enough, it becomes insensitive to this minimal increase, ultimately leading to differences in shape. We conduct additional predictive calculations, increased the calculation precision, and ultimately reduced the error rate, confirming our hypothesis.

Although there is still some residual error. Increasing the computational precision could reduce these errors. The method of constraining shapes through strain in this approach effectively constrains the shape of FBSS. Through the analysis of various shapes, we believe this method is capable of accurately predicting surfaces of any shape, ideally achieving complete shape constraint with no errors.

V. CONCLUSION

This paper proposed a tactile shape sensor based on Fiber-Optic distributed sensors and optimization algorithms. The fibers, arranged in a grid pattern on both sides of a fabric, deform along with the fabric when it undergoes shape changes, generating corresponding strain distributions. We utilized these strain distributions to predict the shape. The primary focus of the article is to introduce and validate the predictive method through simulations.

In the initial data preparation phase, a discrete model for Fabric-Based Shape Sensor (FBSS) is proposed, incorporating specific geometric constraints. Through optimization calculations aimed at minimizing the total potential energy of the FBSS, we successfully derived the sample shape and obtains strain data. In the shape prediction phase, the original geometric constraints are removed, and the optimization calculations are performed again, using the acquired strain data as the sole constraint to derive the predicted shape.

Six sample shapes are considered, ranging from basic bending, twisting, and stretching shapes to concave-convex shapes, such as a single point press, multi-point press (3 points), and reverse press (2 points). The method effectively predicted these shapes, with an average max error rate around

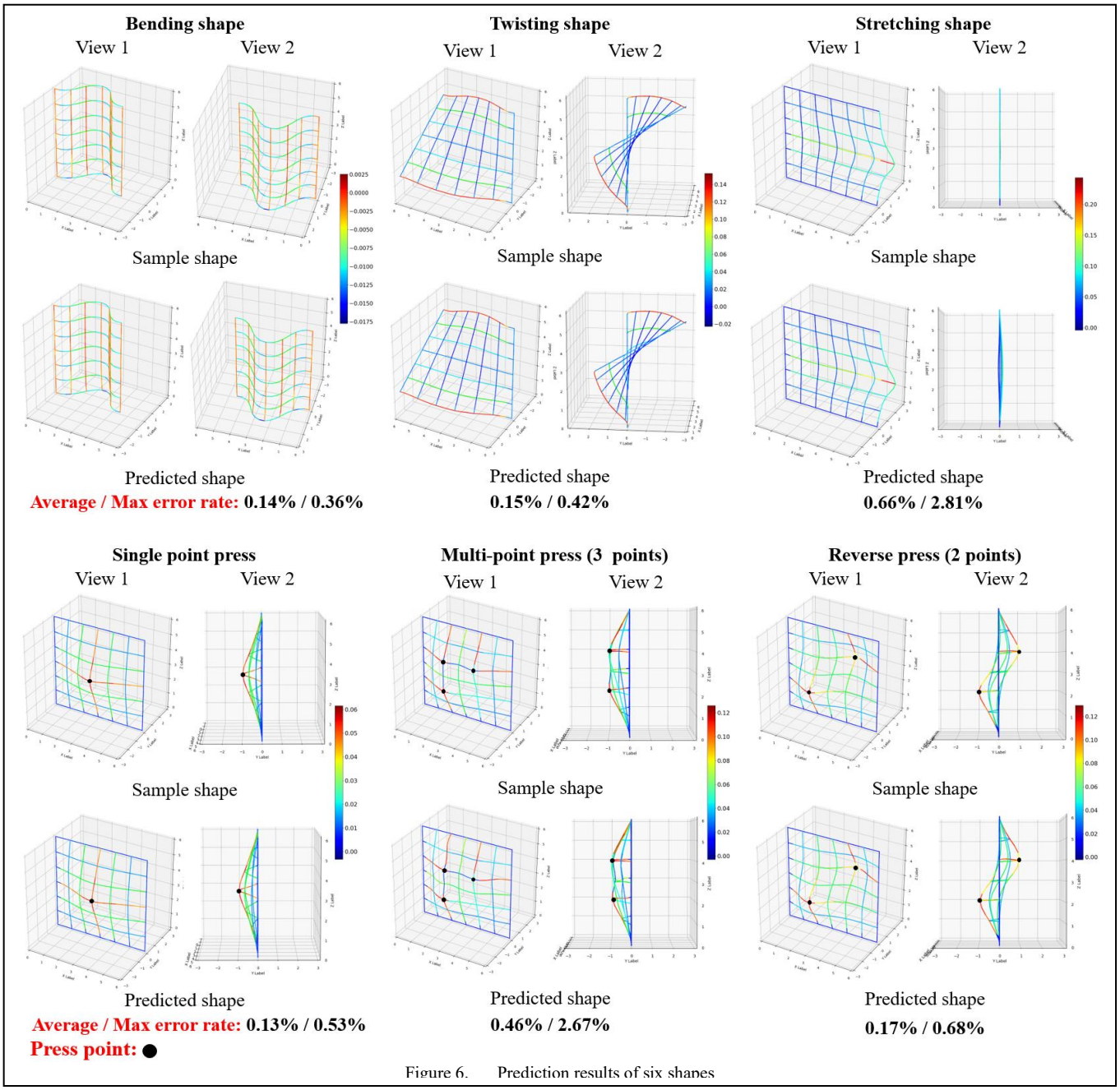

Figure 6. Prediction results of six shapes

2%. These case studies suggest that this predictive method is effective to any complex surfaces.

Future work will involve experimental validation of the predictive method, utilizing the proposed approach to deploy FBSS and conduct predictive calculations based on real strain data. Additionally, this study has limitations in the idealization of the model to reduce computational complexity, and future efforts will focus on developing more accurate models and analyzing the extent of precision loss.

REFERENCES

[1] Y.-F. Liu, "Progress and prospects in flexible tactile sensors," Frontiers in Bioengineering and Biotechnology, vol. 11, Sep. 2023.

[2] Mousavi, "Recent advances in smart wearable sensors as electronic skin," Journal of Materials Chemistry B, vol. 11, no. 43, pp. 10332–10354, Jan. 2023.

[3] Y. Chang, "Recent Advances in Flexible Multifunctional Sensors," Micromachines, vol. 14, no. 11, pp. 2116–2116, Nov. 2023.

[4] D. Shah, "Stretchable Shape-Sensing Sheets," Advanced intelligent systems, vol. 5, no. 12, Oct. 2023.

[5] L. Costi, "Barometric Soft Tactile Sensor for Depth Independent Contact Localization," 2023 IEEE International Conference on Robotics and Biomimetics (ROBIO), Dec. 2023.

[6] X. Bao, "Recent Progress in Distributed Fiber Optic Sensors," Sensors, vol. 12, no. 7, pp. 8601–8639, Jun. 2012.

[7] T. L. T. Lun, "Real-Time Surface Shape Sensing for Soft and Flexible Structures Using Fiber Bragg Gratings," IEEE Robotics and Automation Letters, vol. 4, no. 2, pp. 1454–1461, Apr. 2019.

[8] H. Zhang, "Fiber Bragg grating plate structure shape reconstruction algorithm based on orthogonal curve net," Journal of Intelligent Material Systems and Structures, vol. 27, no. 17, pp. 2416–2425, Jul. 2016.

[9] J. C. Lagarias, "Convergence Properties of the Nelder--Mead Simplex Method in Low Dimensions," SIAM Journal on Optimization, vol. 9, no. 1, pp. 112–147, Jan. 1998.